Report for the Joint Use/Research of the Institute for Planetary Materials, Okayama University for FY2024

05/29/2024r

Category: ☑International Joint Research ☐General Joint Research ☐Joint Use of Facility ☐Workshop

Name of the research project: The effects of pressure, water, and oxygen fugacity on the seismic attenuation of pre-melting polycrystalline olivine in the upper mantle

Principal applicant: Dongliang Jiang

Affiliated institution and department: School of Earth Sciences, Zhejiang University

Collaborator

Name: Baohua Zhang

Affiliated institution and department: School of Earth Sciences, Zhejiang University

Name: Takashi Yoshino

Affiliated institution and department: Institute for Planetary Materials, Okayama University

Research report:

Seismic Attenuation Characteristics of Pre-melting KLB-1 Peridotite in the Upper Mantle

1. Research Background

Seismological observations indicate the presence of globally widespread shear wave velocity reductions and seismic attenuation (with an attenuation factor Q^{-1} exceeding 0.01) in the asthenosphere (Romanowicz and Durek, 2000), located approximately 70 km beneath oceans and 200 km beneath continents (Tauzin et al., 2010; Kawakatsu and Utada, 2017; Debayle et al., 2020; Fischer et al., 2020; Hua et al., 2023). The seismic attenuation in the asthenosphere is associated with a decrease in shear wave velocity (5–10%) (Fischer et al., 2010) and a reduction in viscosity (two orders of magnitude lower than the overlying lithosphere) (Sigmundsson, 1991; Johnson et al., 2007).

The asthenosphere plays a crucial role in geodynamic processes. Its low viscosity allows the relatively rigid lithosphere to move smoothly above it, generating seismic and volcanic activity at plate boundaries and contributing to the stability of tectonic plates, which is essential for plate tectonics (Höink et al., 2012). However, the origin of the asthenosphere remains unresolved.

Partial melting is widely considered the primary cause of the asthenosphere's low viscosity and

reduced seismic wave velocities (Anderson and Spetzler, 1970; Holtzman, 2016; Freitas et al., 2017; Selway and Donnell, 2019). However, this requires a melt fraction of 0.2–3% to wet mineral grain boundaries (Kohlstedt, 1992; Forsyth et al., 1998; Harmon et al., 2011). If the melt does not fully wet the grain boundaries, its connectivity is poor, and its impact on mechanical properties is minimal (Stocker and Gordon, 1975). The effect of partial melting depends on the melt geometry (dihedral angle). For the likely dihedral angles (20–40°) in the shallow asthenosphere, a melt fraction of 3–6% is needed to explain the sharp velocity reduction (5–10%) at the lithosphere-asthenosphere boundary (LAB) (Karato, 2014), which is an order of magnitude higher than the melt fraction generally accepted for mid-ocean ridges. Recent experimental studies suggest that even lower melt fractions (<1%) can significantly affect seismic wave velocities in upper mantle materials. For example, Chantel et al. (2016) showed that ~0.2% melt can reduce shear wave velocities in the asthenosphere by 5–8%, while 0.1% melt confined to triple junctions has almost no effect on seismic properties (P- and S-wave velocities). Although partial melting begins at 100–150 km depth beneath mid-ocean ridges, driven by rising hot material and decompression, aided by volatiles (water/carbon dioxide), the melt production rate at this stage is limited (<0.1%) (Hirschmann, 2010). Even when hot material reaches ~70 km depth, where residual minerals dehydrate and melting can occur without volatile assistance, the melt fraction in regions far from mid-ocean ridges remains below 0.1% (Plank and Langmuir, 1992; McKenzie, 2000). Thus, mechanisms for melt accumulation are necessary. However, it remains challenging to explain the global-scale reduction in seismic wave velocities in the asthenosphere solely through partial melting. For instance, Kawakatsu et al (2009) proposed a layered structure where a small net melt fraction (<1%) in melt-rich layers results in a 10–20% reduction in seismic wave velocities, leading to a decrease in SV (vertically polarized S-wave) velocities. However, the stability of such a structure from a geodynamic perspective is questionable. First, according to Holtzman et al. (2003), deformation-induced melt-rich layers are inclined at ~20° to the shear plane. If melt-rich layers are inclined, gravity would drain the melt, making it difficult to maintain such layers over geological timescales due to efficient compaction. Additionally, this model attributes the velocity reduction to SH/SV shear wave anisotropy, meaning the magnitude of the velocity reduction must equal the magnitude of radial anisotropy ($(V_{SH}-V_{SV})/V_S$=5-10%). While relatively large radial anisotropy has been observed in the central Pacific (Nettles and Dziewonski, 2008), its magnitude is typically less than a few percent in most cases (Beghein et al., 2006). Another model suggests that the LAB may correspond to the depth where melt accumulates due to a permeability barrier, coinciding with the depth where the geotherm intersects the solidus (Hirschmann, 2010). The solidus temperature for water/carbon dioxide-assisted melting is ~1300 K, and in some regions, the LAB depth beneath old oceanic lithosphere (~120 Myr) is ~60 km (Kumar and Kawakatsu, 2011). Standard geothermal models for oceanic upper mantle yield temperatures of 900–1200 K at ~60 km depth (McKenzie et al., 2005; Ritzwoller et al., 2004). Thus, achieving the high temperatures required

for partial melting in old oceanic mantle is challenging.

Other studies propose that water reduces seismic wave velocities through anelastic relaxation, meaning that in regions of the upper mantle with minimal melt fractions, partial melting would lower seismic wave velocities by removing water from minerals like olivine (Karato and Jung, 1998; Mei and Kohlstedt, 2000a, b). Some research indicates that the asthenosphere coincides with the region of minimum water solubility in mantle minerals. Water solubility in aluminous orthopyroxene decreases sharply with depth, while it increases with pressure in olivine (Mierdel et al., 2007). Karato (1995) suggested that the primary role of partial melting may be to remove water from solid minerals, thereby increasing creep strength and affecting other related properties. Hirth and Kohlstedt (1996) expanded this model to study the rheological structure of the oceanic upper mantle, showing that the viscosity of the MORB source region mantle is 500 ± 300 times lower than that of dry olivine aggregates. They proposed that the rheological stratification (lithosphere and asthenosphere) of the oceanic upper mantle may primarily result from stratification in intragranular water content. Thus, the high seismic attenuation, low viscosity, and low shear wave velocities of the asthenosphere could be caused by water weakening of olivine. However, this mechanism has also been questioned recently: experimental results indicate that water has limited effects on the elastic and plastic properties of olivine (Fei et al., 2013), while redox conditions imposed by the choice of metal sample capsules and associated defect chemistry appear to significantly influence seismic properties (Cline II et al., 2016). These findings suggest that elevated water content is not the cause of low-velocity or high-attenuation structures in the upper mantle. The high attenuation observed in hydrous and oxidized regions of the upper mantle (e.g., above subduction zones) may reflect prevalent oxygen fugacity.

In contrast, subsolidus mechanisms in peridotite seem to offer a more plausible explanation for the origin of the asthenosphere. Many researchers argue that anelasticity in solid peridotite near the solidus temperature can induce grain boundary sliding, leading to low velocities without the need for partial melting (Karato, 1993; Gribb and Cooper, 1998; Faul and Jackson, 2005; Stixrude and Lithgow-Bertelloni, 2005; Karato, 2012; Takei, 2017; Ma et al., 2020). When crystals are heated to temperatures close to their melting point, they exhibit "pre-melting" behavior (Humphreys and Dueker, 1994; Priestley and McKenzie, 2006), where the crystal structure becomes significantly distorted (Cantwell et al., 2014), resulting in seismic attenuation, reduced shear wave velocities, and lower viscosity (Hirschmann, 2010; Priestley and McKenzie, 2013). Recent experimental studies by Takei et al. (2014) and Yamauchi and Takei (2016) found that at $T/T_m \leq 0.991$, where partial melting does not occur, anelasticity significantly increases below the solidus temperature in the absence of melt. The anelasticity model derived from their experimental data effectively explains the sharp reduction in seismic shear wave velocities below the dry peridotite solidus in the Pacific mantle, a phenomenon previously unexplained by any model. Given that asthenospheric temperatures are close to the peridotite solidus (Yamauchi and Takei, 2020), olivine pre-melting may be key to the formation

of the asthenosphere. However, experimental challenges have limited understanding of rock anelasticity at seismic frequencies. Previous studies primarily focused on olivine in partially molten states or used rock analogs (organic polycrystals), neglecting pre-melting conditions (Berckhemer et al., 1982; Jackson, 1993; Tan et al., 2001; Jackson et al., 2002; Aizawa et al., 2007; McCarthy and Takei, 2011; McCarthy et al., 2011; Abers et al., 2014).

Seismic attenuation in the mantle results from transient grain-scale dissipation processes driven by stress changes induced by seismic waves. High-pressure and high-temperature experiments provide critical insights into the subsolidus mechanisms responsible for transient creep and attenuation, as well as the influence of temperature, pressure, composition, and grain size. Therefore, in situ measurements of seismic attenuation characteristics of peridotite under pre-melting conditions in the upper mantle are essential for advancing our understanding of the asthenosphere's origin.

2. Research Progress

This study is primarily experimental, utilizing a deformation-DIA (D-DIA) apparatus equipped with a short-period cyclic loading device at the BL04B1 beamline of the SPring-8 synchrotron in Japan to measure seismic attenuation in pre-melting KLB-1 peridotite from the upper mantle. By combining XRD, SEM, and EPMA analyses, we systematically investigate the seismic attenuation characteristics of pre-melting KLB-1 peridotite under high-pressure and high-temperature conditions. To date, we have completed the synthesis of initial minerals and KLB-1 peridotite, determined the solidus of KLB-1 peridotite, and conducted an attenuation experiments (spinel peridotite, 1.5 GPa).

(1) Synthesis of Initial Samples

The initial sample, KLB-1 peridotite, is a spinel lherzolite xenolith from the Kilbourne Hole volcanic crater in New Mexico, USA. Due to its chemical similarity to pyrolite, it is widely regarded as a natural analog for the upper mantle, providing key constraints for understanding mantle melting, seismic wave velocities, and geodynamics. Its mineral composition primarily includes olivine (Ol), orthopyroxene (Opx), clinopyroxene (Cpx), and minor spinel (Sp) or garnet (Gt) (Davis et al., 2009). Different peridotite assemblages reflect their depth of origin. The Ol-Cpx-Opx±Sp±Gt assemblage is stable under upper mantle pressure-temperature conditions, with spinel peridotite transforming to garnet peridotite at pressures >1.5 GPa (Perkins and Anthony, 2011):

$$2\mathrm{Opx}+\mathrm{Cpx}+2\mathrm{Sp}=2\mathrm{Gt}+2\mathrm{Ol} \quad (1)$$

To study the influence of pressure, we synthesized both spinel peridotite and garnet peridotite. The synthesis steps are as follows:

① Synthesis of Ol, Opx, Cpx, Sp, and Gt

The oxide ratios for synthesizing KLB-1 peridotite have been extensively reported (Takahashi and Kushiro, 1983; Takahashi, 1986; Herzberg et al., 1990; Bertka and Holloway, 1994; Baker et al., 1995; Robinson et al., 1998b; Walter, 1998; Wang et al., 2015). The initial oxide ratios used in this study are listed in **Table 1**.

Table 1 Initial Oxide Ratios for KLB-1 Minerals

Initial Mineral	Oxide Ratios (/g)								
	Fe_2O_3	MgO	SiO_2	$CaCO_3$	Al_2O_3	Na_2CO_3	TiO_2	Cr_2O_3	MnO
Ol	0.1086	0.4935	0.4087	/	/	/	/	/	/
Cpx	0.0370	0.1531	0.5233	0.3431	0.0756	0.0295	0.0037	/	/
Opx	0.0767	0.3229	0.5481	0.0145	0.0541	/	/	/	/
Gt	0.0698	0.2006	0.4014	0.0897	0.2217	/	0.0018	0.0102	0.004
Sp	0.1050	0.2120	0.6235	/	/	/	/	0.0700	/

Note:

Ol: $(Mg_{1.8}Fe_{0.2})SiO_4$

Cpx: $(Mg_{0.82}Fe_{0.1}Ca_{0.74}Na_{0.12}Al_{0.2}Ti_{0.01})(Al_{0.12}Si_{1.88})O_6$

Opx: $(Mg_{1.66}Fe_{0.19}Ca_{0.03}Al_{0.12})(Al_{0.1}Si_{1.89})O_6$

Gt: $(Mg_{2.22}Fe_{0.29}Ca_{0.4}Mn_{0.03}Cr_{0.06}Ti_{0.01})(Al_{1.9}Fe_{0.1})(Si_{2.98}Al_{0.04})O_{12}$

Sp: $(Mg_{0.8}Fe_{0.2})(Al_{1.86}Cr_{0.14})O_4$

First, oxide powder mixtures were thoroughly ground for 1 hour in an agate mortar under ethanol, following the ratios in **Table 1**. The mixtures were then pressed into pellets and placed in platinum wire baskets. The pellets were heated in a gas-mixing furnace (**Fig. 1**) at 1200°C under QFM oxygen fugacity (CO_2:H_2 = 285:15) for 2 hours. The baked samples were analyzed using XRD. The results (**Fig. 2**) show high purity for all five minerals, with peaks closely matching standard mineral patterns. Minor impurity peaks were present but at low intensities, confirming suitability for KLB-1 peridotite synthesis.

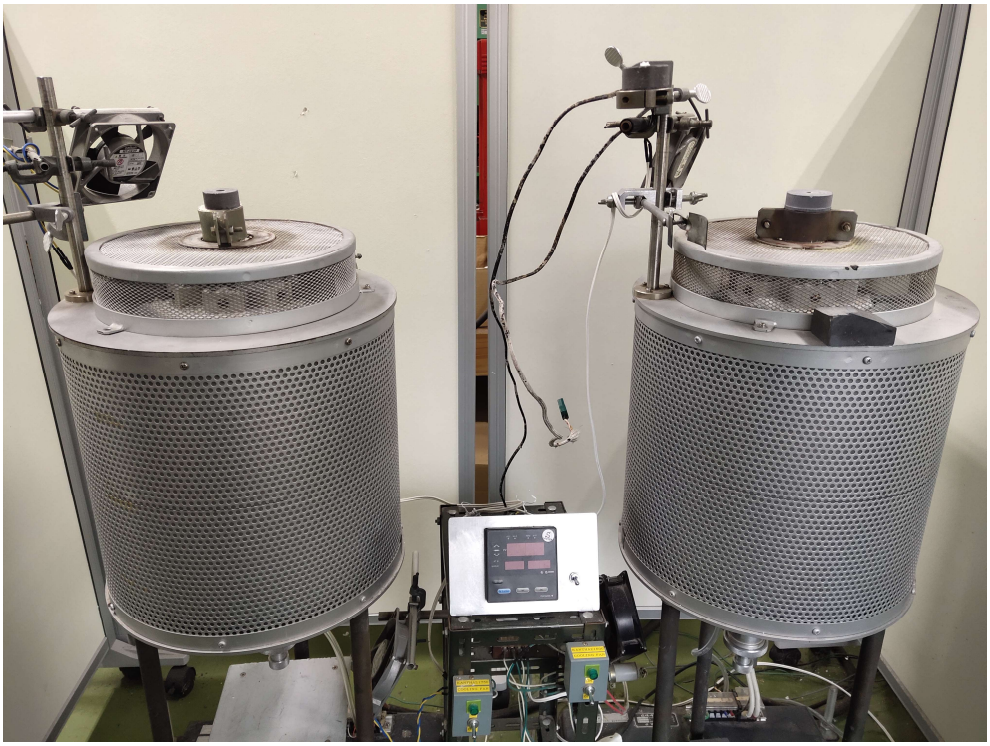

Fig.1 Gas-Mixing Furnace

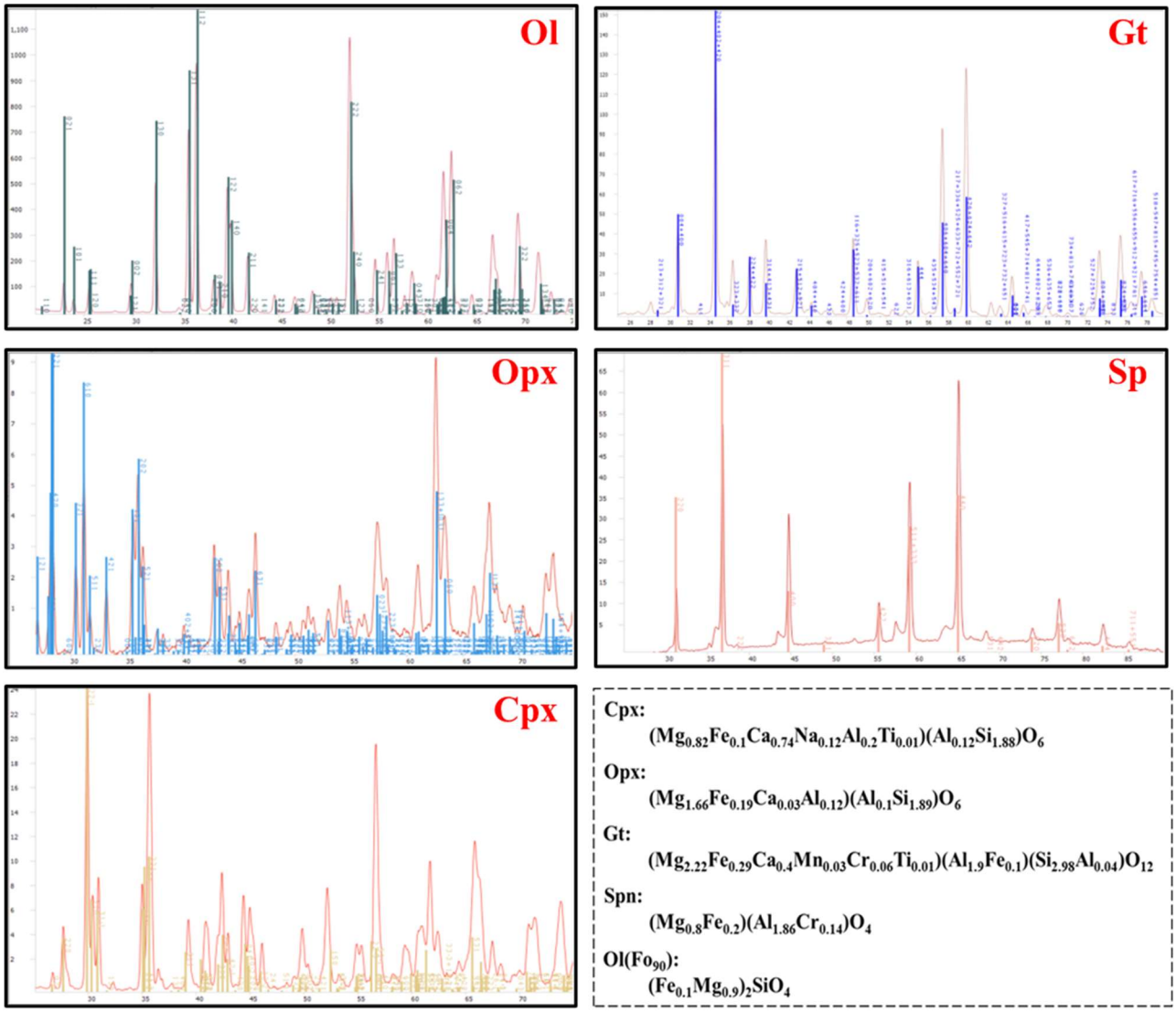

Fig.2 XRD Results for Synthesized Ol, Opx, Cpx, Gt, and Sp

② Synthesis of Spinel Peridotite and Garnet Peridotite

The initial minerals were ground into powder and mixed in the following ratios: (Spinel-peridotite: 59Ol+24Opx +15Cpx +2Sp; garnet-peridotite: 61.5Ol+19Opx +13Cpx +6.5Gt, wt%). The mixtures were ground for 1 hour under ethanol, dried, and loaded into Mo capsules. Using the 25/15 assembly (**Fig.3**), the powders were sintered in a 5000-ton KAWAI-type multi-anvil press (**Fig.4**) at 1.5 GPa and 3 GPa, respectively, and 1200°C to produce spinel peridotite and garnet peridotite. The sintered samples were analyzed for phase and structure using SEM with BSE and EDS capabilities.

The results (**Fig.5** and **Table 2**) show that the major chemical components (FeO, MgO, SiO_2, CaO, Al_2O_3) of the synthesized spinel peridotite and garnet peridotite closely match those of KLB-1 peridotite reported in previous studies (Herzberg et al., 2000), with maximum deviations of only 6.91% for CaO (a minor component at ~3 wt%). Deviations for the major components (MgO and SiO_2) were below 3%, confirming the suitability of the synthesized samples for attenuation experiments.

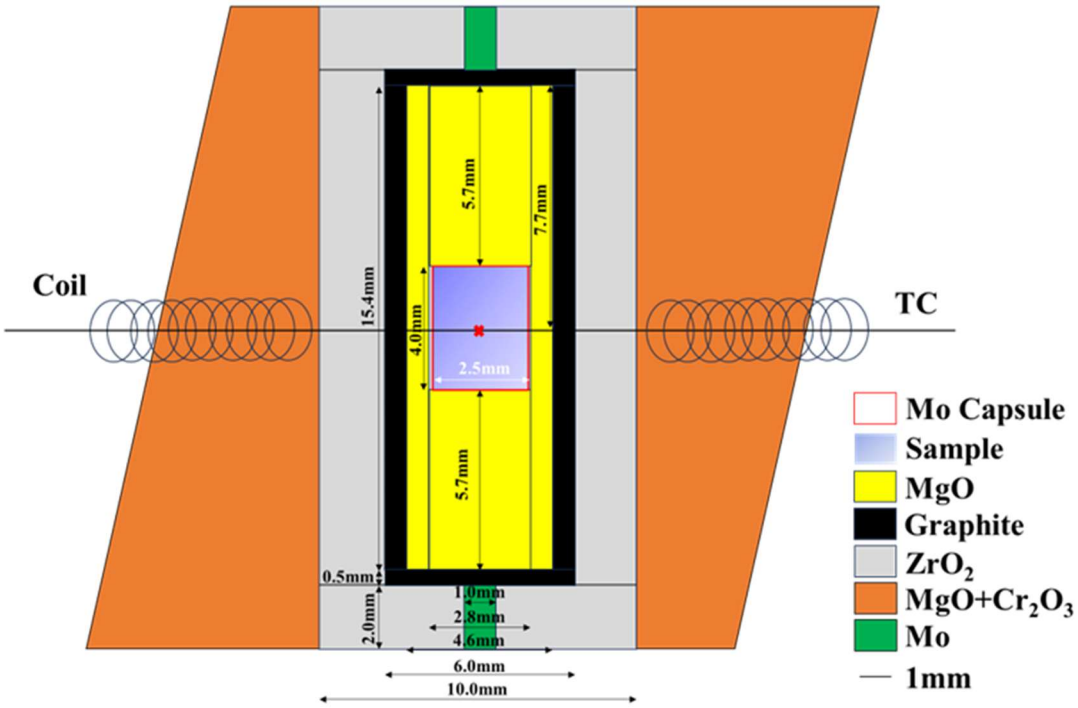

Fig.3 Assembly for KLB-1 Peridotite Synthesis

Fig.4 5000-ton KAWAI-Type Multi-Anvil Press

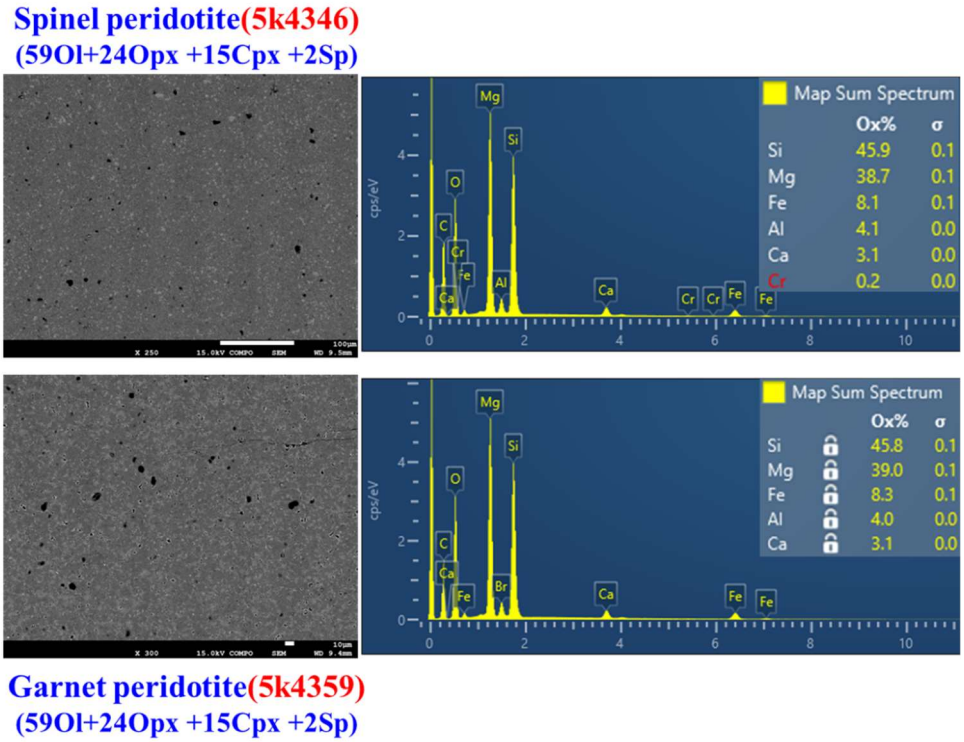

Fig.5 EDS Mapping Results for Recovered Spinel Peridotite and Garnet Peridotite Samples

Table 2 Comparison of Major Chemical Compositions between Synthesized and Previously Studied KLB-1 Peridotite

		FeO, wt%	MgO, wt%	SiO_2, wt%	CaO, wt%	Al_2O_3, wt%
Previous Studies (Avg)		8.19	38.47	44.89	3.33	4.09
This study	Spinel peridotite	8.10	38.70	45.90	3.10	4.10
	Deviation, %	1.10	0.60	2.25	6.91	0.24
	Garnet peridotite	8.30	39.00	45.80	3.10	4.00
	Deviation, %	1.34	1.38	2.03	6.91	2.20

(2) Determining Solidus of Initial Sample

As shown in **Fig.6**, the solidus of spinel peridotite and garnet peridotite were determined using a piston-cylinder apparatus with a 1/2-inch assembly. Experimental parameters, including temperature, pressure, and duration, are listed in Table 3. BSE imaging was used to identify melt formation, and mineral/melt compositions were measured (**Fig.7** and **8**). The results indicate solidus of ~1250°C for spinel peridotite and ~1450°C for garnet peridotite, consistent with previous studies (e.g., Herzberg et al (2000) reported solidus of ~1300°C at 1.5 GPa and ~1500°C at 3 GPa for KLB-1 peridotite). The ~50°C discrepancy may arise from differences in iron content.

Table 3 Solidus Determination Experiments

Sample	No.	T,℃	P，GPa	t，min	Melt	Solidus，℃
Spinel peridotite	PC1220	1320	1.5	180	√	~1250
	PC1221	1260	1.5	180	√	
	PC1222	1230	1.5	180	×	
Garnet peridotite	PC1207	1700	3.0	15	√	~1450
	PC1211	1520	3.0	15	√	
	PC1214	1490	3.0	15	√	
	PC1212	1460	3.0	15	√	
	PC1217	1440	3.0	180	×	
	PC1205	1400	3.0	15	×	

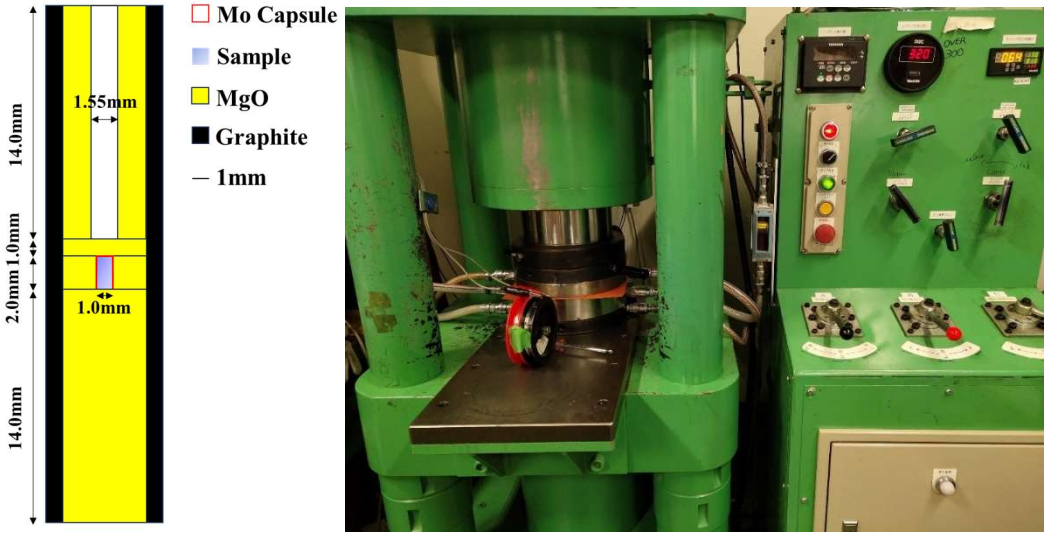

Fig.6 Schematic of Solidus Experiment Assembly and Piston-Cylinder Apparatus

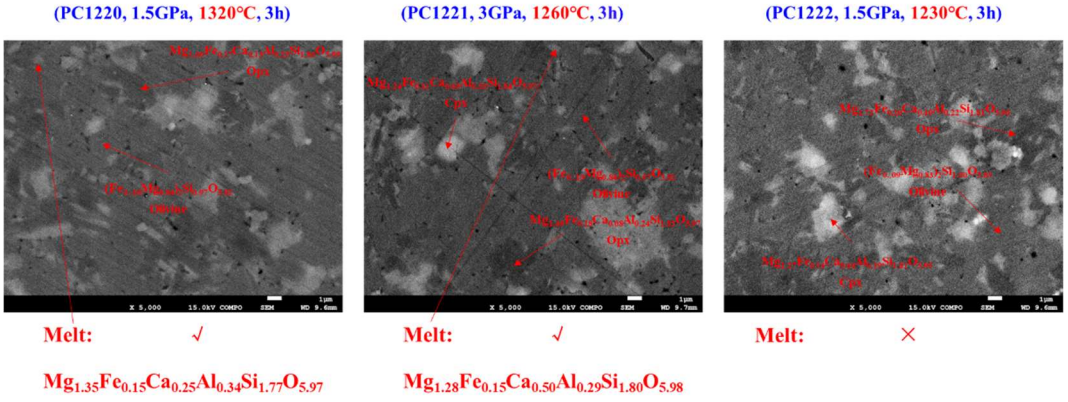

Fig.7 EDS Results for Recovered Spinel Peridotite Sample

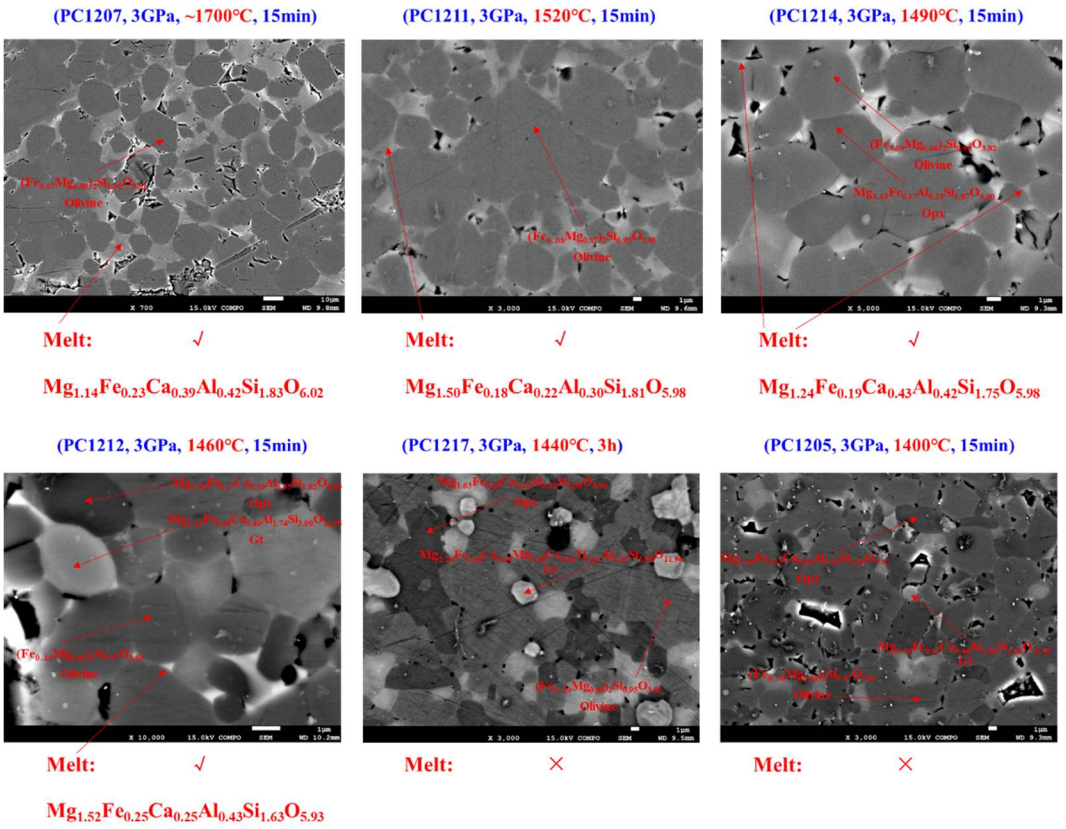

Fig.8 EDS Results for Recovered Garnet Peridotite Sample

(3) Attenuation Experiments and Data Analysis

The attenuation experiments employed a 10/6 assembly (**Fig.9**), with MgO + Cr_2O_3 as the pressure medium. A graphite heater surrounded by zirconia insulation was used to elevate the system temperature. MgO tubes replaced insulation layers to serve as X-ray windows (MgO absorbs far less X-rays than zirconia). MgO also reduced temperature gradients in the sample chamber. Samples and references were encased in BN, with alumina pistons at the top and bottom to balance deformation and pressure transfer efficiency from the D-DIA anvils. To enhance contrast in X-ray imaging, 20 μm-thick Pt foils were placed between samples, pistons, and references. Temperature was monitored using D-type thermocouples ($W_{97}Re_3$-$W_{75}Re_{25}$).

Forced oscillation experiments were conducted using a D-DIA apparatus installed at the BL04B1 beamline of SPring-8. The optical system is shown in **Fig.10**. White light passed through the multi-anvil press and was imaged on a CMOS camera or diffracted on a solid-state detector (SSD). Sample diffraction was used for phase identification and pressure calculation. Strain was measured via X-ray imaging, and diffraction patterns were obtained using the SSD. Secondary anvils were fixed with chemically processed wood guides. Camera positioning was adjusted from far (>2 m) to near (<1 m), significantly improving image quality (contrast between materials) and enabling clearer identification of sample and reference boundaries.

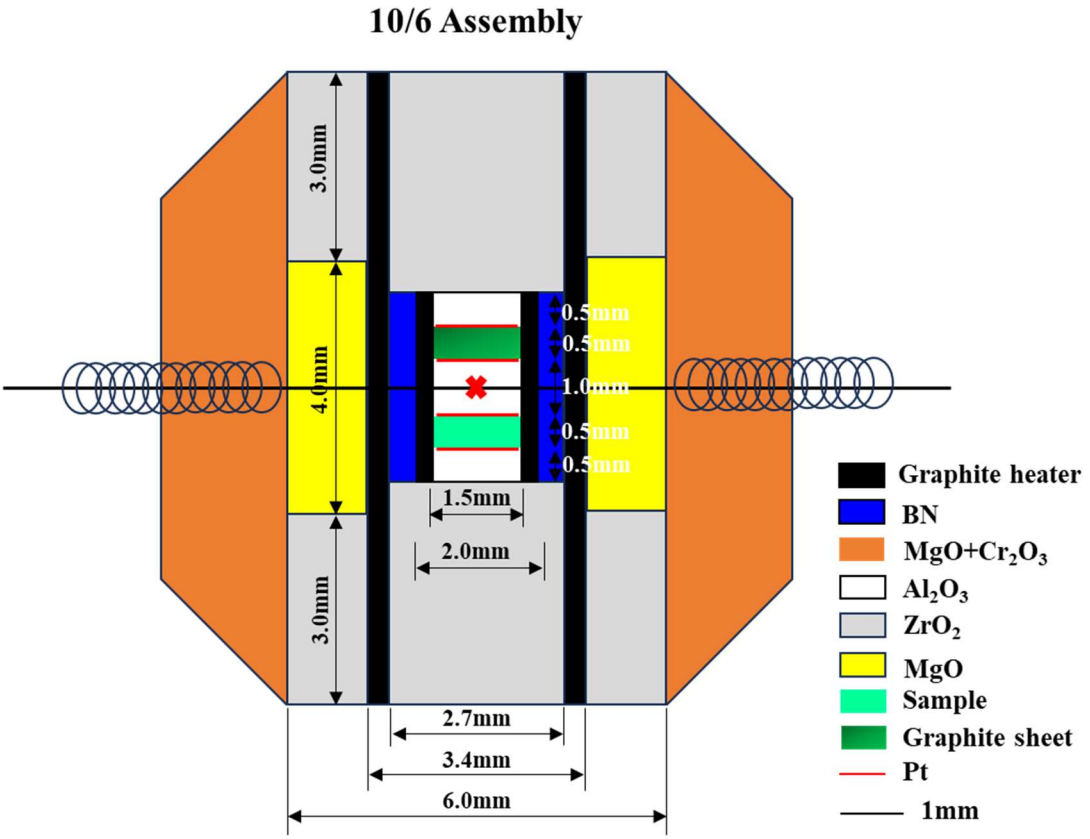

Fig.9 Forced Oscillation Attenuation Experiment Assembly

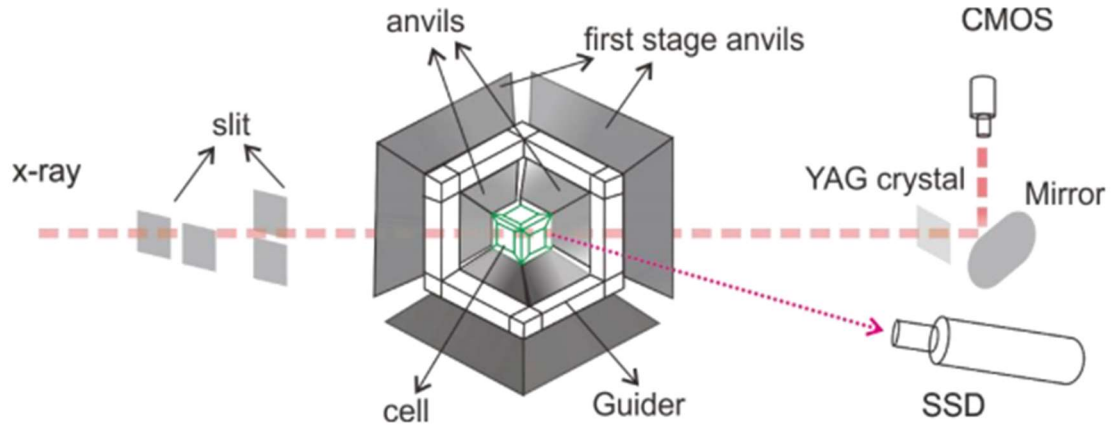

Fig.10 SPring-8 Optical System

Experiments were conducted at 1.5 GPa, with imaging before and after pressurization (0 tons and 40 tons, respectively; **Fig.11**). A comparison of the assembly before and after the experiment is shown in **Fig.12**. Temperatures tested were 800°C, 1100°C, 1150°C, 1175°C, 1200°C, 1220°C, 1230°C, 1240°C, 1250°C, 1260°C, 1275°C, 1300°C, and room temperature. At each temperature, oscillation periods ranged from 0.5 to 1000 s (0.5, 1, 2, 5, 10, 20, 50, 100, 300, 1000 s), covering most observed seismic wave ranges.

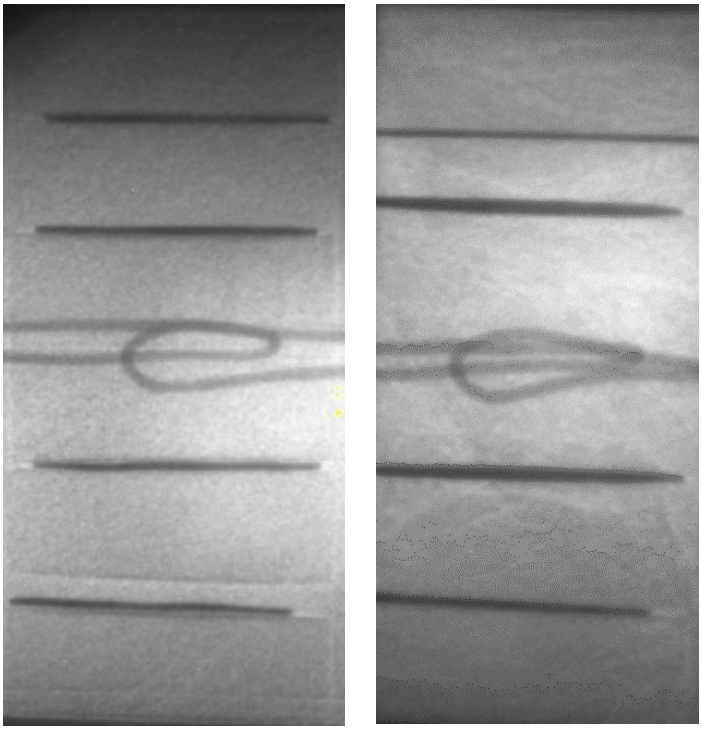

Fig.11 Imaging Before (0 tons, left) and After (40 tons, right) Pressurization

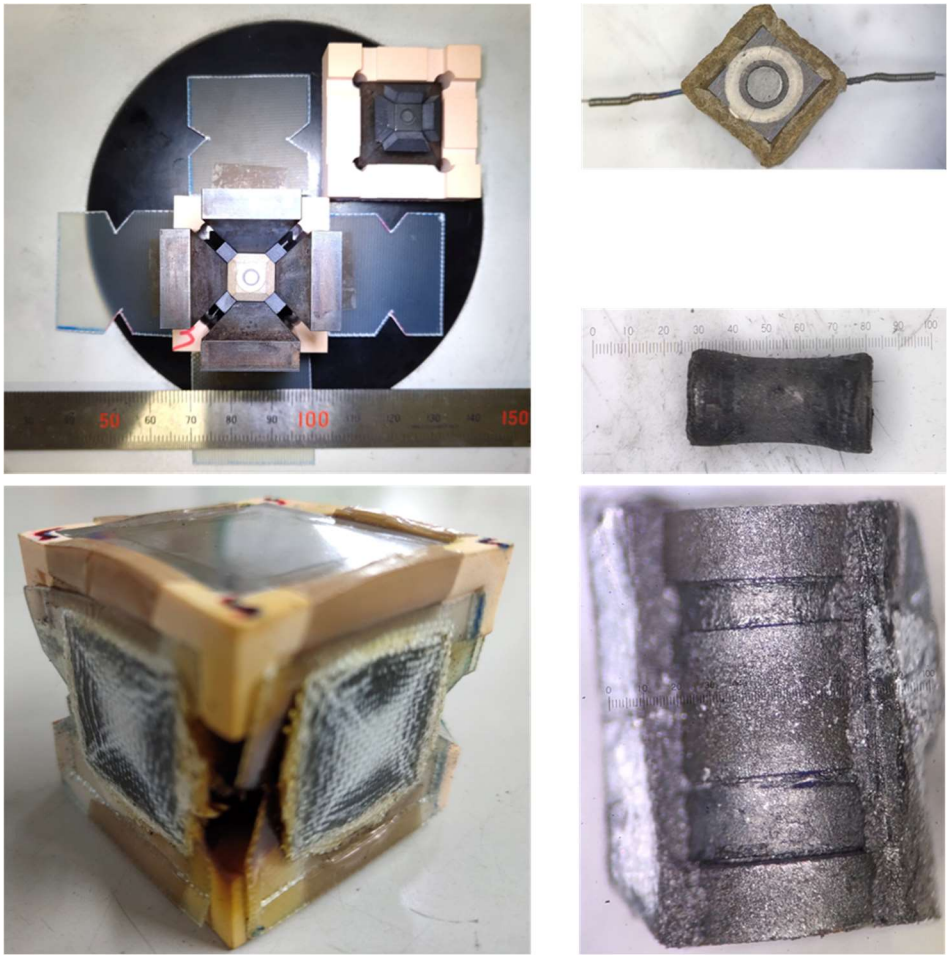

Fig.12 Assembly Comparison Before and After Attenuation Experiment

Attenuation is grain-size-dependent: at higher frequencies or lower temperatures, grain boundary sliding is accommodated by elastic deformation of adjacent grains, manifesting as recoverable anelastic behavior with weak attenuation. As temperature increases or periods lengthen, diffusion processes dominate, and grain boundary sliding is accommodated by material diffusion, leading to irreversible viscous strain and enhanced attenuation. Smaller grain sizes shorten diffusion paths, making attenuation more sensitive to grain size (Jackson et al., 2002). Thus, grain size statistics before and after experiments are necessary. As shown in **Fig.13**, 561 grain sizes were measured for sample 5k4346 before the attenuation experiment, showing a normal distribution with an average grain size of 1.87 μm. For recovered sample M4518, 639 grains were measured (**Fig.14**), showing a normal distribution with an average grain size of 4.13 μm. **Fig.15** and **16** show grain size statistics for each mineral before and after the attenuation experiment. Before the experiment, Ol + Opx (indistinguishable in contrast, counted together) had an average grain size of 2.12 μm, and Cpx averaged 1.56 μm. After the experiment, Ol, Opx, and Cpx averaged 5.01 μm, 4.06 μm, and 2.68 μm, respectively, showing ~2× growth. However, the average grain size remained at 4.13 μm, confirming the reliability of the attenuation data.

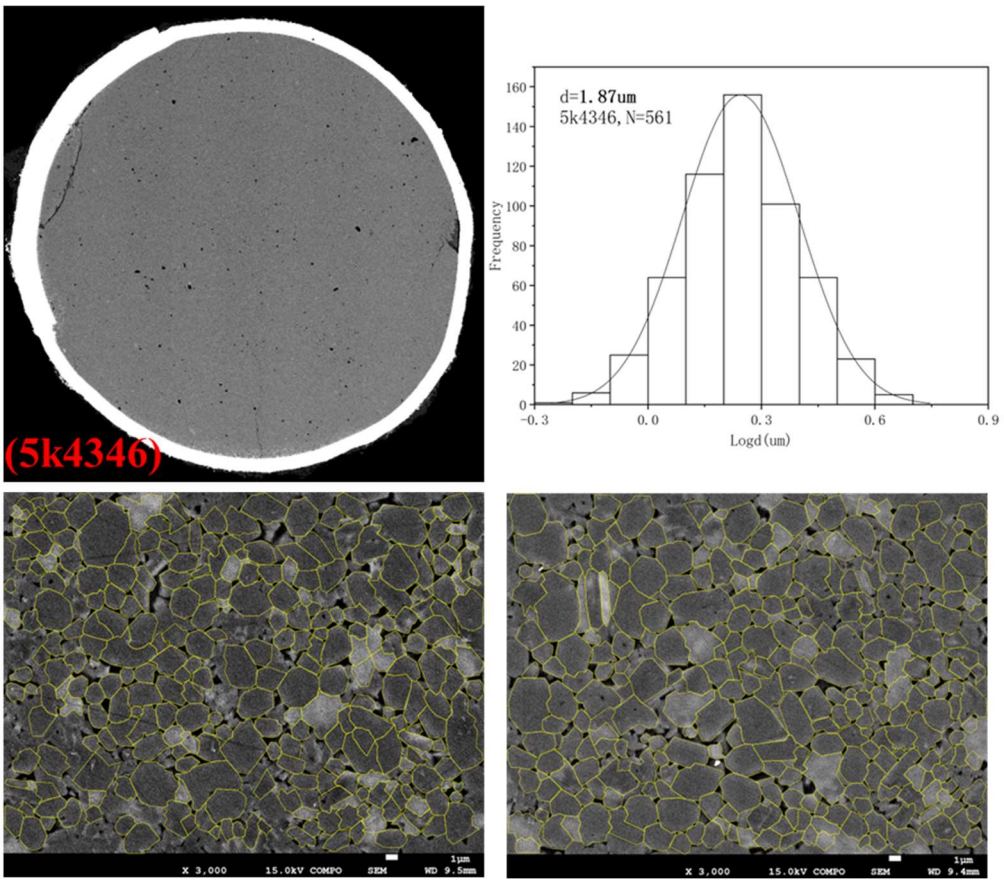

Fig.13 Grain Size Distribution Before Attenuation Experiment

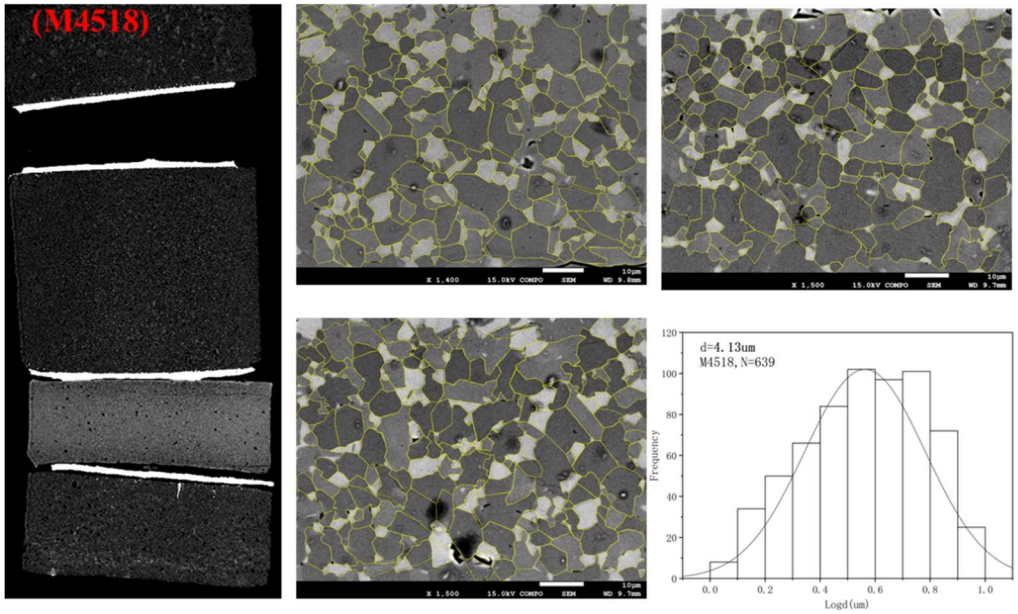

Fig.14 Grain Size Distribution After Attenuation Experiment

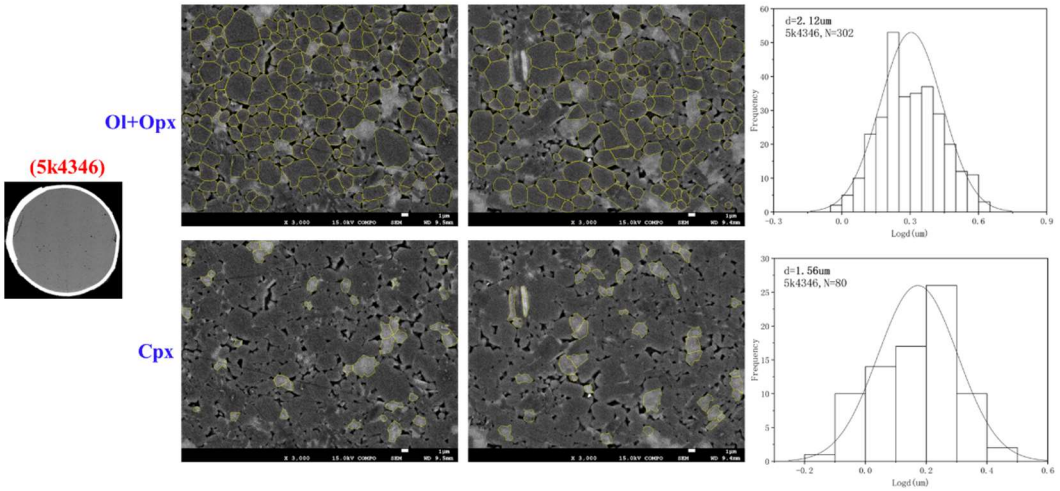

Fig.15 Grain Size Distribution by Mineral Before Attenuation Experiment

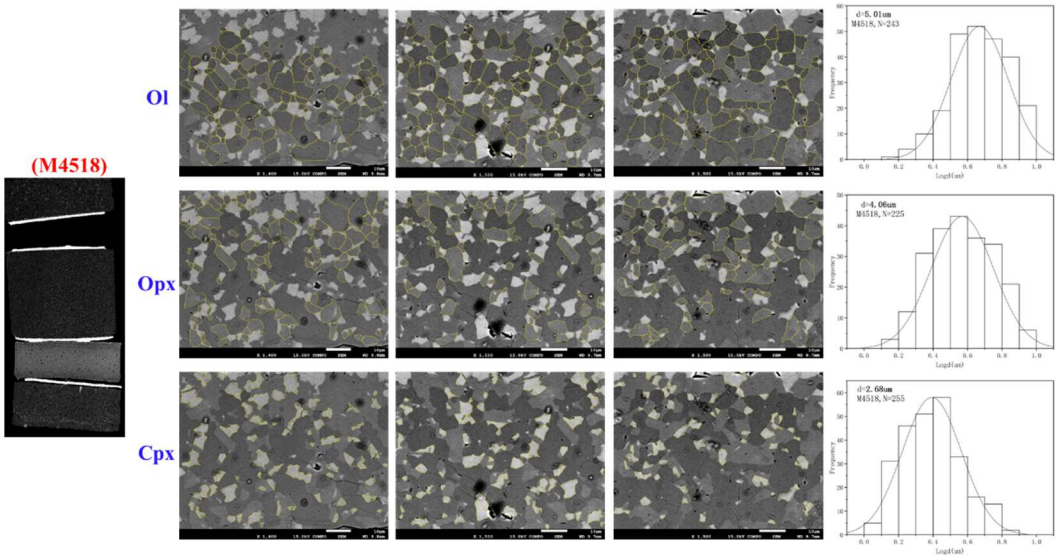

Fig.16 Grain Size Distribution by Mineral After Attenuation Experiment

As shown in **Fig.17**, with increasing temperature, Log(Q^{-1}) at the attenuation peak (Log(Period) ≈ 20s) increases. When the temperature reaches the pre-melting state ($0.97T_m \leqslant T < T_m$), i.e., starting from 1220°C, Log(Q^{-1}) shows a significant increase, indicating markedly enhanced attenuation under pre*melting conditions. Beyond the solidus (>1250℃), the emergence of melt also leads to a pronounced increase in Log(Q^{-1}). However, due to the temperature gradient between the measurement point and the sample, the loss of iron from the sample to the Pt strain markers at both ends (See below "**3. Existing Issues and Proposed Solutions**"), and errors in the calculation of the attenuation factor, the data require further cleaning and analysis, which will be addressed in subsequent experiments.

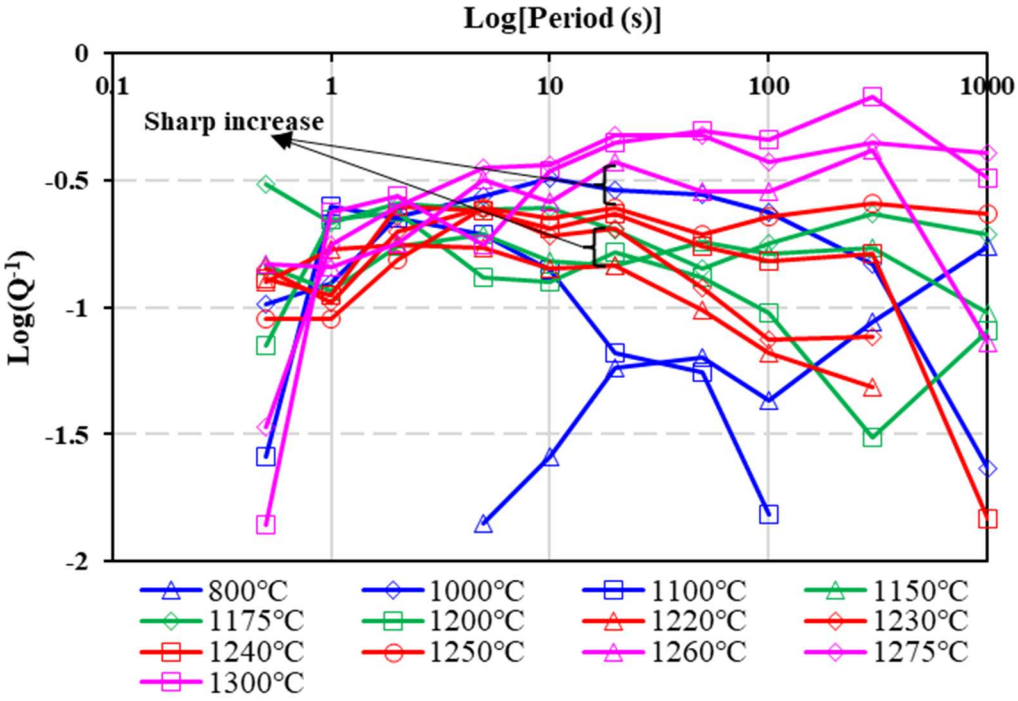

Fig.17 The Variation of Attenuation Factor with Period at Different Temperatures

3. Existing Issues and Proposed Solutions

(1) Temperature Gradient in Attenuation Experiment Assembly

As shown in **Fig.9**, the thermocouple in the attenuation experiment measures temperature at the assembly's center, not the sample position. The distance between the measurement point and the sample center is 0.75 mm. Given the focus on pre-melting conditions, temperature accuracy is critical. To address this, a temperature gradient measurement assembly was designed (**Fig.18**), featuring two thermocouples placed at the assembly center and the sample center, respectively, to determine the temperature gradient between these points under experimental conditions.

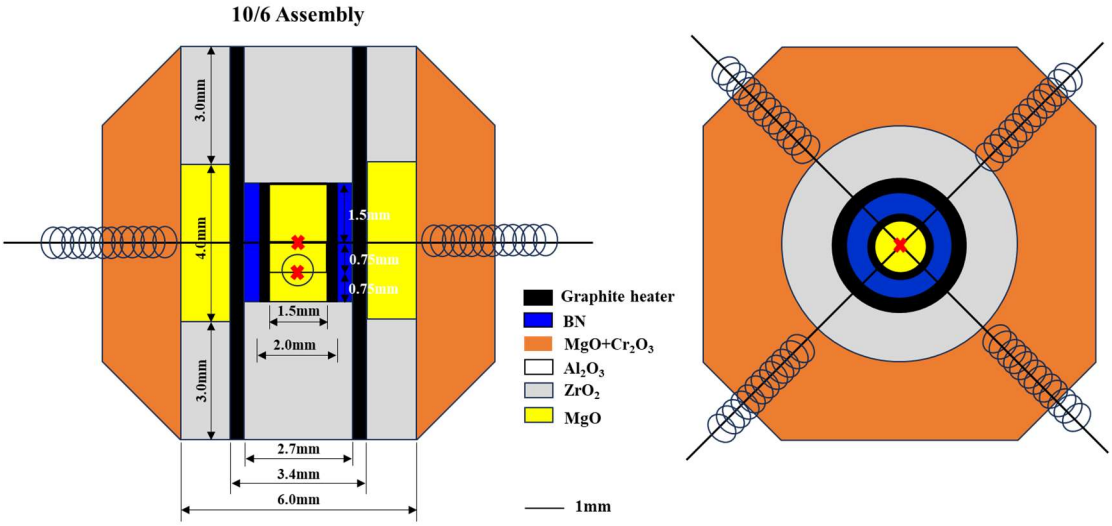

Fig.18 Schematic of Temperature Gradient Measurement Assembly

(2) Iron Loss in Samples

In high-pressure-temperature experiments, samples are typically encapsulated in noble metal capsules. Previous studies show that Fe and other metallic elements readily alloy with noble metals, leading to significant loss of these elements from the sample. As shown in **Fig.19**, BSE and EDS analyses of recovered samples reveal that regions near the Pt strain markers (A and C) are darker than the central region (B), indicating Fe loss toward the ends. Fe oxide content in A and C regions was 2.1% and 2.7%, respectively, significantly lower than the initial sample (8.1%). Even in region B, Fe oxide content was 5.8%, still notably reduced. Pt area scans (region D) showed 92.1% Pt and 7.9% Fe oxide, confirming Fe migration into Pt. This loss results from charge interactions between Pt and silicates: FeO is reduced from the silicate melt to form FePt alloy, releasing excess O_2 (Grove, 1982).

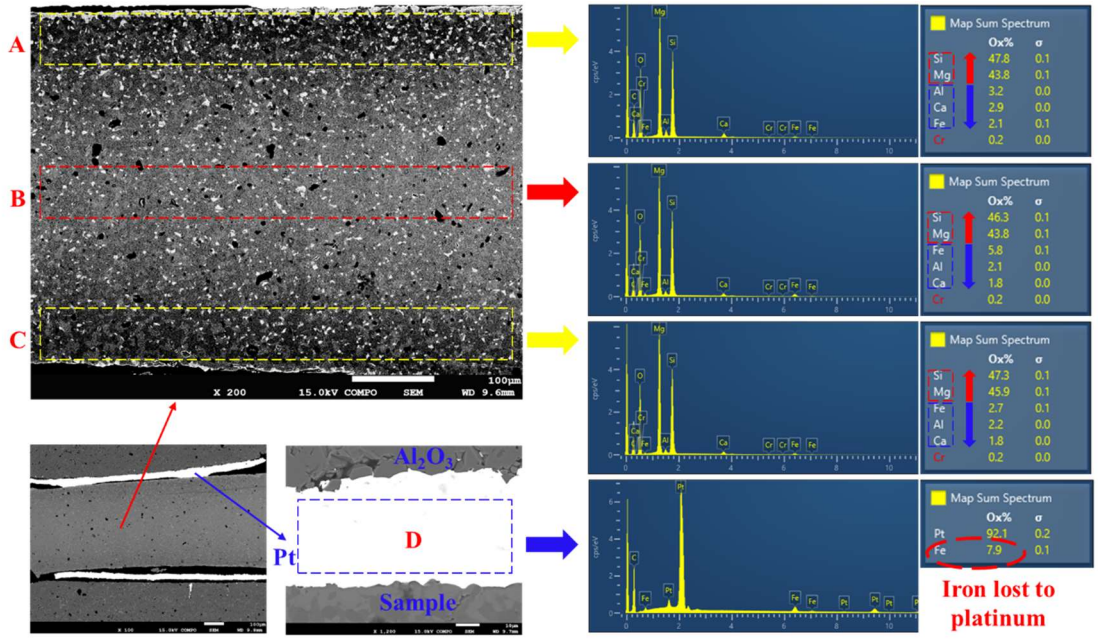

Fig. 19 The Iron Loss in Recovered Sample

Wang et al. (2020) conducted experiments at 1 GPa, 1400°C, and FMQ-2 to FMQ+5 oxygen fugacity using Pt, graphite-lined Pt, and Re-lined Pt capsules. Results demonstrated that graphite and Re liners physically isolate starting materials from Pt, effectively preventing Fe loss. Additionally, pre-saturation techniques significantly reduce Fe loss in Pt, with FePt alloy containing 6–10 wt% Fe under QFM conditions (Grove, 1982).

Thus, we designed a piston-cylinder assembly (**Fig.20**). First, Fe and Pt powders (8 wt% + 92 wt%) were mixed under ethanol, loaded into BN capsule, and sintered at 1300°C and 1.5 GPa for 6 hours to form FePt alloy (**Fig.20a**). The alloy was analyzed via XRD and EDS to confirm composition. The synthesized FePt alloy was rolled into 20 μm foils, and FePt, Re, and Mo discs (1.4 mm diameter) were laser-cut as strain markers. Using the assembly in **Fig20.b**, reactions were conducted at 1300°C and 1.5 GPa for 24 hours to measure Fe loss from spinel peridotite into FePt, Re, and Mo, identifying the optimal marker material to prevent Fe loss.

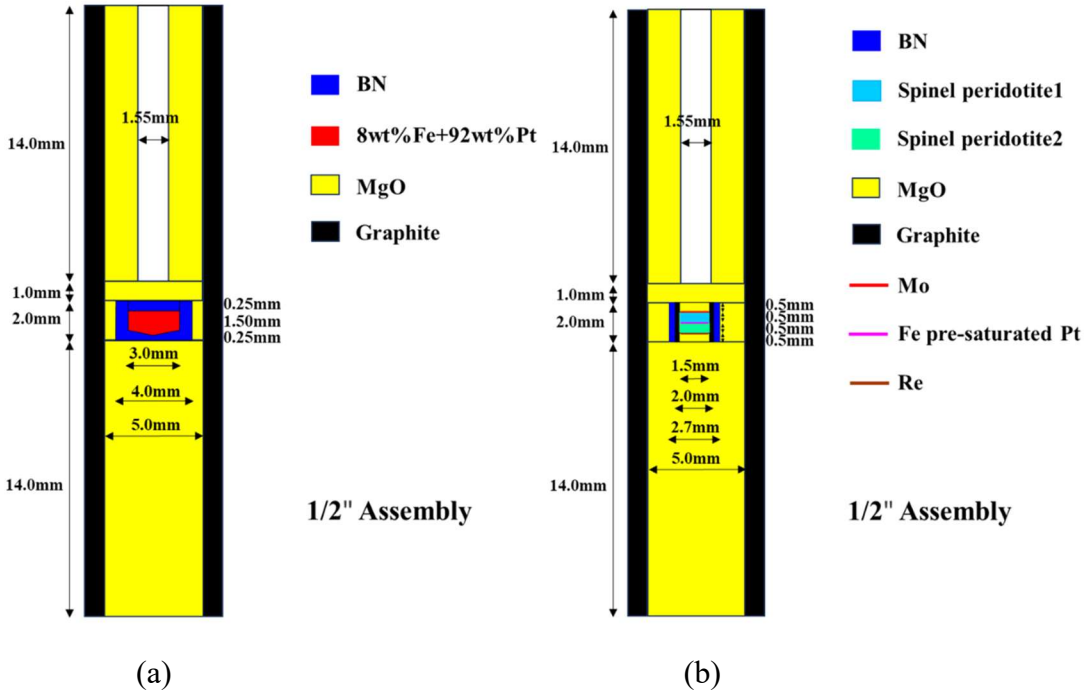

(a) (b)

Fig.20 Assembly for The Synthesis of FePt Alloy (a) and for Verifying The Loss of Iron from The Sample to Different Metals (b)

4. Next Plans

(1) Processing data from attenuation experiment M4518 to calculate the relationship between attenuation factor Q^{-1} and period at different temperatures, and to determine shear modulus and wave velocity changes.

(2) Determining the temperature gradient between the sample and measurement points in the attenuation experiment assembly.

(3) Synthesizing Fe-pre-saturated FePt alloy for strain markers.

(4) Conducting optimized attenuation experiments on spinel peridotite and garnet peridotite.

References

Abers, G.A., Fischer, K., Hirth, M.G., et al., 2014. Reconciling mantle attenuation-temperature relationships from seismology, petrology, and laboratory measurements. Geochem. Geophys. Geosyst., 15(9), 3521–3542. https://doi.org/10.1002/2014GC005444

Aizawa, Y., Barnhoorn, A., Faul, U.H., et al., 2007. Seismic properties of Anita Bay dunite: An exploratory study of the influence of water. J. Petrol., 49(4), 841–855. https://doi.org/10.1093/PETROLOGY%2FEGN007

Anderson, D.L., Spetzler, H., 1970. Partial melting and the low-velocity zone. Phys. Earth Planet. In., 4, 62–64. https://doi.org/10.1016/0031-9201(70)90030-0

Baker, M.B., Hirschmann, M.M. Ghiorso, M.S., et al., 1995. Compositions of near-solidus peridotite melts from experiments and thermodynamic calculations. Nature, 375, 308–311. https://doi.org/10.1038/375308a0

Beghein, C., Trampert, J., Van Heijst, H.J., 2006. Radial anisotropy in seismic reference models of the mantle. J. Geophys. Res.: Solid Earth, 111. https://doi.org/10.1029/2005JB003728

Berckhemer, H., Kampfmann, W., Aulbach, E., et al., 1982. Shear modulus and Q of forsterite and dunite near partial melting from forced-oscillation experiments. Phys. Earth Planet. Inter., 29(1), 30–41. https://doi.org/10.1016/0031-9201(82)90135-2.

Bertka, C.M., Holloway, J.R., 1994. Anhydrous partial melting of an iron-rich mantle I: subsolidus phase assemblages and partial melting phase relations at 10 to 30 kbar. Contr. Mineral. and Petrol., 115, 313–322. https://doi.org/10.1007/BF00310770

Cantwell, P.R., Tang, M., Dillon, S.J., et al., 2014. Grain boundary complexions. Acta Mater., 62, 1–48. https://doi.org/10.1016/j.actamat.2013.07.037

Chantel, J., Manthilake, G., Andrault, D., et al., 2016. Experimental evidence supports mantle partial melting in the asthenosphere. Sci. Adv., 2(5), Article e1600246. https://doi.org/10.1126/sciadv.1600246

Cline II, C., Faul, U., David, E., et al., 2018. Redox-influenced seismic properties of upper-mantle olivine. Nature, 555, 355–358. https://doi.org/10.1038/nature25764

Davis, F.A., Tangeman, J.A., Tenner, T.J., et al., 2009. The composition of KLB-1 peridotite. Am. Min., 94 (1), 176–3180. https://doi.org/10.2138/am.2009.2984

Debayle, E., Bodin, T., Durand, S., et al., 2020. Seismic evidence for partial melt below tectonic plates. Nature, 586, 555–559. https://doi.org/10.1038/s41586-020-2809-4

Faul, U.H., Jackson, I., 2005. The seismological signature of temperature and grain size variations in the upper mantle. Earth Planet. Sci. Lett., 234, 119–34. https://doi.org/10.1016/J.EPSL.2005.02.008

Fei, H., Wiedenbeck, M., Yamazaki, D., et al., 2013. Small effect of water on upper-mantle rheology based on silicon self-diffusion coefficients. Nature, 498, 213–215. https://doi.org/10.1038/nature12193

Fischer, K.M., Rychert, C.A., Dalton, C.A., et al., 2020. A comparison of oceanic and continental mantle lithosphere. Phy. Earth Planet. In., 309, 106600. https://doi.org/10.1016/j.pepi.2020.106600

Fischer, K.M., Ford, H.A., Abt, D.L., et al., 2010. The lithosphere-asthenosphere boundary. Annu. Rev. Earth Planet. Sci., 38, 551–575. https://doi.org/10.1146/annurev-earth-040809-152438

Forsyth, D.W., et al., 1998. Imaging the deep seismic structure beneath a mid-ocean ridge: The melt experiment. Science, 280(5367), 1215–1218. https://doi.org/10.1126/science.280.5367.1215

Freitas, D., Manthilake, G., Schiavi, F. et al., 2017. Experimental evidence supporting a global melt layer at the base of the Earth's upper mantle. Nat Commun., 8, 2186. https://doi.org/10.1038/s41467-017-02275-9

Gribb, T.T., Cooper, R.F., 1998. Low-frequency shear attenuation in polycrystalline olivine: grain boundary diffusion and the physical significance of the Andrade model for viscoelastic rheology. J. Geophys. Res.: Solid Earth, 103, B1127267–79. https://doi.org/10.1029/98JB02786

Grove, T.L., 1982. Use of FePt alloys to eliminate the iron loss problem in 1 atmosphere gas mixing experiments: Theoretical and practical considerations. Contr. Mineral. and Petrol., 78, 298–304. https://doi.org/10.1007/BF00398924

Harmon, N., Forsyth, D.W., Weeraratne, D.S., et al., 2011. Mantle heterogeneity and off axis volcanism on young Pacific lithosphere. Earth Planet. Sci. Lett., 311(3–4), 306–315. https://doi.org/10.1016/j.epsl.2011.09.038

Hirschmann, M.M., 2010. Partial melt in the oceanic low velocity zone. Phys. Earth Planet. Inter., 179(1–2), 60–71. https://doi.org/10.1016/j.pepi.2009.12.003

Herzberg, C., Gasparik, T., Sawamoto, H., 1990. Origin of mantle peridotite: Constraints from melting experiments to 16.5 GPa. J. Geophys. Res.: Solid Earth, 95, 15779–15803. https://doi.org/10.1029/JB095iB10p15779

Herzberg, C., Raterron, P., Zhang, J.Z., 2000. New experimental observations on the anhydrous solidus for peridotite KLB-1. Geochem. Geophys. Geosyst., 11(1). https://doi.org/10.1029/2000GC000089

Hirth, G., Kohlstedt, D.L., 1996. Water in the oceanic upper mantle: Implications for rheology, melt extraction and the evolution of the lithosphere. Earth Planet. Sci. Lett., 144(1–2), 93–108. https://doi.org/10.1016/0012-821X(96)00154-9

Höink, T., Lenardic, A., Richards, M., 2012. Depth-dependent viscosity and mantle stress

amplification: implications for the role of the asthenosphere in maintaining plate tectonics. Geophys. J. Int., 191, 30–41. https://doi.org/10.1111/j.1365-246X.2012.05621.x

Holtzman, B.K., 2016. Questions on the existence, persistence, and mechanical efects of a very small melt fraction in the asthenosphere. Geochem. Geophys. Geosyst., 17, 470–484. https://doi.org/10.1002/2015GC006102

Holtzman, B.K., Kohlstedt, D.L., Zimmerman, M.E., et al., 2003. Melt segregation and strain partitioning: implications for seismic anisotropy and mantle flow. Science, 301, 1227–1230. https://doi.org/10.1126/science.1087132

Hua, J., Fischer, K.M., Becker, T.W., et al., 2023. Asthenospheric low-velocity zone consistent with globally prevalent partial melting. Nat. Geosci., 16, 175–181. https://doi.org/10.1038/s41561-022-01116-9

Humphreys E.D., Dueker K.G., 1994. Physical state of the western US upper mantle. J. Geophys. Res.: Solid Earth, 99(B5), 9635–9650. https://doi.org/10.1029/93JB02640

Jackson, I., 1993. Progress in the experimental study of seismic wave attenuation. Annu. Rev. Earth Planet. Sci., 21, 375–406. https://doi.org/10.1146/annurev.ea.21.050193.002111

Jackson, I., Fitz Gerald, J.D., Faul, U.H., et al., 2002. Grain-size-sensitive seismic wave attenuation in polycrystalline olivine. J. Geophys. Res.: Solid Earth, 107(B12), 2360. https://doi.org/10.1029/2001JB001225

Johnson, K.M., Hilley, G.E., Bürgmann, R., 2007. Influence of lithosphere viscosity structure on estimates of fault slip rate in the Mojave region of the San Andreas fault system. J. Geophys. Res.: Solid Earth, 112, B07408. https://doi.org/10.1029/2006JB004842

Karato, S.I., 1993. Importance of anelasticity in the interpretation of seismic tomography. Geophys. Res. Lett., 20, 1623–1626. https://doi.org/10.1029/93GL01767

Karato, S.I., 1995. Effects of water on seismic wave velocities in the upper mantle. Proc. Jpn. Acad.,

70, 61-66. https://doi.org/10.2183/pjab.71.61

Karato, S.I., Jung, H., 1998. Water, partial melting and the origin of the seismic low velocity and high attenuation zone in the upper mantle. Earth Planet. Sci. Lett., 157(3–4), 193–207. https://doi.org/10.1016/S0012-821X%2898%2900034-X

Karato, S.I., 2012. On the origin of the asthenosphere. Earth Planet. Sci. Lett., 321–322, 95-103. https://doi.org/10.1016/j.epsl.2012.01.001

Karato, S.I., 2014. Does partial melting explain geophysical anomalies? Phys. Earth Planet. Inter., 228, 300-306. https://doi.org/10.1016/j.pepi.2013.08.006

Kawakatsu, H., Kumar, P., Takei, Y., et al., 2009. Seismic evidence for sharp lithosphere–asthenosphere boundaries of oceanic plates. Science, 324, 499-502. https://doi.org/10.1126/science.1169499

Kawakatsu, H., Utada, H., 2017. Seismic and electrical signatures of the lithosphere–asthenosphere system of the normal oceanic mantle. Annu. Rev. Earth Planet. Sci., 45, 139-167. https://doi.org/10.1146/ANNUREV-EARTH-063016-020319

Kohlstedt, D.L., 1992. Structure, rheology and permeability of partially molten rocks at low melt fractions. In mantle flow and melt generation at mid-ocean ridges (eds Morgan, J.P., Blackman, D.K., and Sinton, J.M.), Washington, D.C.: Trans. Am. Geophys., 103–121. https://doi.org/10.1029/GM071p0103

Kumar, P., Kawakatsu, H., 2011. Imaging the seismic lithosphere–asthenosphere boundary of the oceanic plate. Geochem. Geophys. Geosyst., 12. https://doi.org/10.1029/2010GC003358

Liu, C., Yoshino, T., Yamazaki, D., et al., 2021. Exploration of the best reference material on anelastic measurement by cyclic loading under high pressure. High Press. Res., 42(1), 14–28. https://doi.org/10.1080/08957959.2021.2013834

Ma, Z., Dalton, C.A., Russell, J.B., et al., 2020. Shear attenuation and anelastic mechanisms in the

central Pacific upper mantle. Earth Planet. Sci. Lett., 536, 116148. https://doi.org/10.1016/j.epsl.2020.116148

McKenzie, D., 2000. Constraints on melt generation and transport from U-series activity ratios. Chem. Geol., 162(2), 81–94. https://doi.org/10.1016/S0009-2541(99)00126-6

McCarthy, C., Takei, Y., 2011. Anelasticity and viscosity of partially molten rock analogue: toward seismic detection of small quantities of melt. Geophys. Res. Lett., 38, L18306. https://doi.org/10.1029/2011GL048776

McCarthy, C., Takei, Y., Hiraga, T., 2011. Experimental study of attenuation and dispersion over a broad frequency range: 2. The universal scaling of polycrystalline materials. J. Geophys. Res.: Solid Earth, 116, B09207. https://doi.org/10.1029/2011JB008384

McKenzie, D., Jackson, J.A., Priestley, K., 2005. Thermal structure of oceanic and continental lithosphere. Earth Planet. Sci. Lett., 233, 337–349. https://doi.org/10.1016/j.epsl.2005.02.005

Mei, S., Kohlstedt, D.L., 2000a. Influence of water on plastic deformation of olivine aggregates. 1. Diffusion creep regime. J. Geophys. Res.: Solid Earth, 105, 57–69. https://doi.org/10.1029/2000JB900179

Mei, S., Kohlstedt, D.L., 2000b. Influence of water on plastic deformation of olivine aggregates. 2. Dislocation creep regime. J. Geophys. Res.: Solid Earth, 105, 71–81. https://doi.org/10.1029/2000JB900180

Mierdel, K., Keppler, H., Smyth, J.R., et al., 2007. Water Solubility in Aluminous Orthopyroxene and the Origin of Earth's Asthenosphere. Science, 315, 364–368. https://doi.org/10.1126/science.1135422

Nettles, M., Dziewonski, A.M., 2008. Radially anisotropic shear velocity structure of the upper mantle globally and beneath North America. J. Geophys. Res.: Solid Earth, 113. https://doi.org/10.1029/2006JB004819

Perkins, D., Anthony, E.Y., 2011. The evolution of spinel lherzolite xenoliths and the nature of the mantle at Kilbourne Hole, New Mexico. Contrib. Mineral. Petrol., 162, 1139–1157. https://doi.org/10.1007/s00410-011-0644-1

Perrillat, J.P., Bonjan, R., Godec, Y.L., et al., 2021. A new high-pressure technique for the measurement of low frequency seismic attenuation using cyclic torsional loading. Rev. Sci. Instrum., 92(9), 093906. https://doi.org/10.1063/5.0055549

Plank, T., Langmuir, A.H., 1992. Effects of melting regime on the composition of the oceanic crust. J. Geophys. Res.: Solid Earth, 97(B13), 19749–19770. https://doi.org/10.1029/92JB01769

Priestley, K., McKenzie, D., 2006. The thermal structure of the lithosphere from shear wave velocities. Earth Planet. Sci. Lett., 244(1–2), 285–301. https://doi.org/10.1016/j.epsl.2006.01.008

Priestley, K., McKenzie, D., 2013. The relationship between shear wave velocity, temperature, attenuation and viscosity in the shallow part of the mantle. Earth Planet. Sci. Lett., 381, 78–91. https://doi.org/10.1016/j.epsl.2013.08.022

Ritzwoller, M.H., Shapiro, N.M., Zhong, S., 2004. Cooling history of the Pacific litho-sphere. Earth Planet. Sci. Lett., 226, 69–84. https://doi.org/10.1016/j.epsl.2004.07.032

Robinson, J.A.C., Wood, B.J., 1998a. The depth of the spinel to garnet transition at the peridotite solidus, Earth Planet. Sci. Lett., 164(1-2), 277–284. https://doi.org/10.1016/S0012-821X(98)00213-1

Robinson, J.A.C., Wood, B.J., Blundy, J.D.,1998b. The beginning of melting of fertile and depleted peridotite at 1.5 GPa, Earth Planet. Sci. Lett., 155(1-2), 97–111. https://doi.org/10.1016/S0012-821X(97)00162-3

Romanowicz, B., Durek, J.J., 2000. Seismological constraints on attenuation in the Earth: A review. In Earth's deep interior: mineral physics and tomography from the atomic to the global scale (eds Karato, S., Forte, A., Liebermann, R., Masters, G., and Stixrude, L.), Washington, D.C.: Trans.

Am. Geophys., 161–179. https://doi.org/10.1029/GM117p0161

Selway, K., O'Donnell, J.P., 2019. A small, unextractable melt fraction as the cause for the low velocity zone. Earth Planet. Sci. Lett., 517, 117–124. https://doi.org/10.1016/j.epsl.2019.04.012

Sigmundsson, F., 1991. Post-glacial rebound and asthenosphere viscosity in Iceland. Geophys. Res. Lett., 18(6), 1131–1134. https://doi.org/10.1029/91GL01342

Stixrude, L., and Lithgow-Bertelloni, C., 2005. Mineralogy and elasticity of the oceanic upper mantle: origin of the low-velocity zone. J. Geophys. Res.: Solid Earth, 110, B03204. https://doi.org/10.1029/2004JB002965

Stocker, R.L., Gordon, R.B., 1975. Velocity and internal friction in partial melts. J. Geophys. Res.: Solid Earth, 80, 4828–4836. https://doi.org/10.1029/JB080i035p04828

Takahashi, E., 1986. Melting of a dry peridotite KLB-1 up to 14 GPa: Implications on the Origin of peridotitic upper mantle. J. Geophys. Res.: Solid Earth, 91, 9367–9382. https://doi.org/10.1029/JB091iB09p09367

Takahashi, E., Kushiro, I., 1983. Melting of a dry peridotite at high pressures and basalt magma genesis. Am. Min., 68(9-10), 859–879.

Takei, Y., 2017. Effects of partial melting on seismic velocity and attenuation: a new insight from experiments. Annu. Rev. Earth Planet. Sci., 45(1), 447–470. https://doi.org/10.1146/annurev-earth-063016-015820

Takei, Y., Karasawa, F., Yamauchi, H., 2014. Temperature, grain size, and chemical controls on polycrystal anelasticity over a broad frequency range extending into the seismic range. J. Geophys. Res.: Solid Earth, 119, 5414–5443. https://doi.org/10.1002/2014JB011146

Tan, B., Jackson, I., Fitz Gerald, J.D., 2001. High-temperature viscoelasticity of fine-grained polycrystalline olivine. Phys. Chem. Min., 28, 641–664. https://doi.org/10.1007/s002690100189

Tauzin, B., Debayle, E., Wittlinger, G., 2010. Seismic evidence for a global low-velocity layer within

the Earth's upper mantle. Nat. Geosci., 3, 718–721. https://doi.org/10.1038/ngeo969

Walter, M.J., 1998. Melting of garnet peridotite and the origin of komatiite and depleted lithosphere. J Petrol., 39, 29–60. https://doi.org/10.1093/petroj/39.1.29

Wang, J.T, Xiong, X.L., Zhang, L., er al., 2020. Element loss to platinum capsules in high-temperature – pressure experiments. Am. Mineral., 105(10), 1593–1597. https://doi.org/10.2138/am-2020-7580

Wang, X.B., Chen, T., Zou, Y.T., et al., 2015. Elastic wave velocities of peridotite KLB-1 at mantle pressures and implications for mantle velocity modeling. Geophys. Res. Lett., 41, 3289–3297. https://doi.org/10.1002/2015GL063436

Yamauchi, H., Takei, Y., 2016. Polycrystal anelasticity at near-solidus temperatures. J. Geophys. Res.: Solid Earth, 121, 7790–7820. https://doi.org/10.1002/2016JB013316

Yamauchi, H., Takei, Y., 2020. Application of a premelting model to the lithosphere-asthenosphere boundary. Geochem. Geophys. Geosyst., 21, e2020GC009338. https://doi.org/10.1029/2020GC009338